scientific reports

Check for updates

OPEN

High throughput screen identifies lysosomal acid phosphatase 2 (ACP2) to regulate IFN-1 responses to potentiate oncolytic VSVΔ51 activity

Boaz Wong[1,2], Rayanna Birtch[1,2], Anabel Bergeron[1,2], Kristy Ng[1], Glib Maznyi[1], Marcus Spinelli[1], Andrew Chen[1], Anne Landry[1,2], Mathieu J. F. Crupi[1,2], Rozanne Arulanandam[1], Carolina S. Ilkow[1,2] & Jean-Simon Diallo[1,2]✉

Strategies in genetic and pharmacological modulation of innate immunity to enhance oncolytic virotherapy (OV) efficacy are being explored. We have recently characterized the ability for vanadium-based compounds, a class of pan-phosphatase (PP) inhibitors, to potentiate OVs. We next sought to identify PPs that could be targeted to enhance OVs, akin to vanadium. By conducting a high-throughput screen of a library of silencing RNA (siRNA) targeting human PPs, we uncovered several PPs that robustly enhanced infectivity and oncolysis of the oncolytic vesicular stomatitis virus (VSVΔ51). Knockdown of our top validated hit, lysosomal acid phosphatase 2 (ACP2), increased VSVΔ51 viral titers by over 20-fold. In silico analysis by RNA sequencing revealed ACP2 to regulate antiviral type I interferon (IFN-1) signaling pathways, similar to vanadium. To further exploit this mechanism for therapeutic gain, we encoded a short-hairpin RNA (shRNA) against ACP2 into oncolytic vesicular stomatitis virus (VSVΔ51) under a miR-30 promoter. This bioengineered OV demonstrated expression of the miR-30 promoter, knockdown of ACP2, repression and ultimately, showed markedly enhanced viral VSVΔ51 particle production compared to its non-targeting control counterpart. Altogether, this study identifies IFN-1 regulating PP targets, namely ACP2, that may prove instrumental in increasing the therapeutic efficacy of OVs.

Keywords Oncolytic virotherapy, Phosphatase, High-throughput screening, Genetic silencing, Bioengineering, Interferon

Since its discovery as a potent anti-tumor agent in the 1950s, the development of viruses as a cancer immunotherapy has escalated in recent decades highlighted by the clinical approval of talimogene laherparepvec (T-VEC) for the treatment of melanoma in 2015[1,2]. Through genetic engineering, oncolytic virotherapy (OV) promises potent cancer cell killing and the development of robust anti-tumor immunological memory, all while leaving physiological tissue unharmed[3]. This efficacy hinges upon the innate type 1 interferon (IFN-1) response, which orchestrates the initial propagation of cellular antiviral programs and bridging to inflammatory processes[4]. While most tumors have been thought to be deficient in this IFN-1 response as a byproduct of malignant transformation, residual IFN-1 responses have been blamed for therapeutic resistance to OV regimens[5]. Thus, the genetic or pharmacological modulation of cellular processes that ultimately impinge upon the IFN-1 response represents a logical strategy to improve the therapeutic gain of OVs[6,7]. To this end, our group identified vanadium-based compounds, among others, to improve the viral spread, bystander killing and anti-tumor efficacy of OVs, such as the oncolytic vesicular stomatitis virus (VSVΔ51), when administered in combination[8]. This mechanism was eventually found to be secondary to activation of the epidermal growth factor receptor (EGFR) subsequently leading to changes in STAT phosphorylation and NF-κB signaling to

[1]Centre for Innovative Cancer Research, Ottawa Hospital Research Institute, Ottawa, ON K1H 8L6, Canada. [2]Department of Biochemistry, Microbiology and Immunology, Faculty of Medicine, University of Ottawa, Ottawa, ON K1H 8M5, Canada. ✉email: jsdiallo@ohri.ca

subvert IFN-1 responses towards more of an IFN-2 phenotype[9]. However, given the well-known pan-protein phosphatase (PP) inhibitory activity of vanadium, the exact PPs responsible for this phenomenon remain elusive.

Protein phosphorylation represents a major post-translational regulatory mechanism; therefore, its imbalance typically results in disruption of key cellular functions. The covalent addition of a phosphate group by kinases triggers conformational changes to its respective substrate thereby changing its response, typically towards activation[10]. PPs are responsible for the removal of phosphates to reverse this regulation, therefore, their inhibition often culminates in substrate hyperactivation, as in the case of constitutive EGFR activity upon vanadium treatment[9]. Given their extensive regulation across a plethora of cellular processes, interception of a few PPs has unsurprisingly been demonstrated to both enhance and antagonize IFN-1 responses. Through dephosphorylation of IFN-binding receptors, protein tyrosine phosphatase 1B (PTP1B) stimulates their endocytic turnover to repress antiviral response and defenses[11]. On the other hand, there is evidence that phosphatase slingshot homolog protein 1 (SHP-1) controls the secretion of IFN-1 effectors and pro-inflammatory cytokines[12]. Without the use of a high-throughput screening approach, there are undoubtedly many more involved PP targets to be discovered.

In an attempt to increase OV potency and selectivity, various payloads have been encoded into the genomic backbone of viral vectors[13]. These typically consist of immunomodulatory transgenes, such as interferon gamma (IFN-ɣ) or interleukin-12, intended to elicit stronger anti-tumor immune responses[14,15]. The use of RNA interference (RNAi) has recently led to the investigation of another potential class of payloads for delivery by viral vectors for cancer therapy. Through the delivery of RNAi effectors which include silencing RNA (siRNA) and microRNA (miRNA), the expression of specific gene transcripts can be dramatically reduced for therapeutic gain. Broadly, these RNAi effectors can elicit similar effects as virus encoded transgenes from immunomodulation to induction of tumor cell apoptosis to direct oncogene silencing[16]. Although the majority of in vivo tested viral-delivered RNAi are by replication incompetent vectors, the synergy between RNAi effectors and the inherent oncolytic ability of replication-competent viruses represents a promising avenue for investigation.

The objective of this study was to identify PP targets that could mimic the OV-enhancing effects of vanadium and its respective mechanism of action in regulating the innate antiviral response. Upon successful identification of an OV-enhancing PP target, we then aimed to express RNAi against the identified PP as a payload using a VSVΔ51 vector to develop a bioengineered OV with increased viral infectivity and oncolytic activity.

Results

High-throughput siRNA phosphatase screen identifies candidates for OV enhancement

To identify protein phosphatases (PP) that play a regulatory role in the cellular antiviral defense, we employed a high-throughput screening (HTS) approach using the MISSION® silencing RNA (siRNA) Human Phosphatase Library targeting 303 phosphatase genes using an arsenal of 1,131 total siRNA. 786-0 cells were selected as the cellular model given its natural resistance to VSVΔ51 infection, which would highlight any phosphatases that would enhance VSVΔ51 infectivity upon knockdown. 786-0 cells were seeded in 96well plates and transfected with respective siRNA at a concentration of 0.2μM using Invitrogen's Lipofectamine® RNAiMAX reagent, then infected with oncolytic vesicular stomatitis virus (VSVΔ51) tagged with firefly luciferase (FLuc). Following 48 h of incubation, samples were titered using a previously established high-throughput method and relative cell viability was established using resazurin metabolic dye (Fig. 1A)[17]. Each siRNA was assigned calculated values expressed as (1) fold-change in viral titer over infected cells transfected with a universal negative control and (2) oncolysis enhancing factor defined as the logarithm of the viability of transfected cells divided by the viability of transfected infected cells. As a positive control, siRNA against retinoic acid-inducible gene I (RIG-I), central to innate antiviral interferon (IFN) signaling[18], and cells treated with vanadate were used.

Each siRNA target was plotted for its viability when combined with VSVΔ51 and significance in P-value when compared to cells treated only with control siRNA (Fig. S2). A total of 232 of the 1,131 tested targets were able to significantly decrease the cell viability below 40% with a P-value less than 0.05 (upper left quadrant). To score viability, an *oncolysis enhancing factor* was assigned to each library siRNA target which considers the cytotoxicity generated from the siRNA in the absence of VSVΔ51 infection and gives a positive score to targets that synergize with VSVΔ51 for increased oncolysis. Given that the average oncolysis enhancing factor for vanadate treated samples is 0.43 (blue points in Fig. 1B), a total of 54 PP targets scored higher than vanadate with the highest hit being slingshot homolog 3 (SSH3). Similarly, in Fig. 1C, the fold-change in VSVΔ51 viral titer with PP siRNA transfection was plotted for each target against significance in P-value compared to cells treated with control siRNA. The HTS found 78 targets situated in the upper right quadrant with viral titer fold-change greater than 1.5 and P-value less than 0.05. The HTS found that the target with the greatest increase in viral titer was protein phosphatase 1, regulatory subunit 16 A (PPP1R16A) which increased VSVΔ51 viral titer by about 3-fold. To combine the results of both measures to determine the top candidates of the HTS, oncolysis enhancing factor and fold-change in viral titer were plotted together in Fig. 1D. Using the previously selected cutoffs of oncolysis enhancing factor greater than 0.43 and fold-change in viral titer greater than 1.5, this identified 38 hits, which are shown in Table 1. These candidates were subsequently selected for validation.

Knockdown of ACP2 enhances VSVΔ51 infectivity and oncolysis

For the validation of top PP targets in Table 1, we transfected the top siRNA identified from the library into 786-0 cells, then infected with VSVΔ51 tagged with green fluorescent protein (GFP) to directly visualize the viral enhancing impact of the siRNA. Fluorescent foci were counted and fold change was calculated relative to control cells treated with scramble siRNA. The validation demonstrated that only two hits were able to increase VSVΔ51 greater than vanadate: lysosomal acid phosphatase 2 (ACP2) and phosphoserine phosphatase (PSPH) by 19.5 and 17.5-fold respectively (Fig. 2A). We ultimately selected to proceed with ACP2 given its greatest increase in VSVΔ51 viral titer on validation. To confirm its genetic knockdown using custom sequence siRNA (outlined in

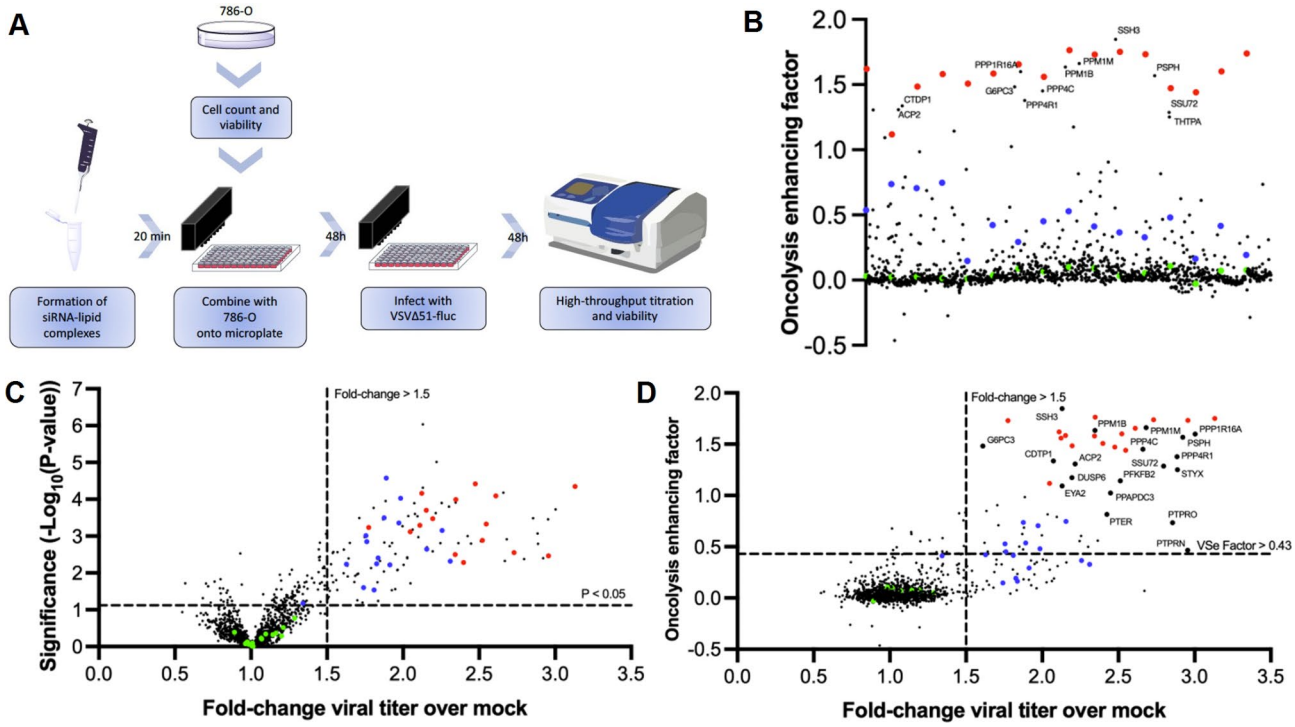

Fig. 1. High throughput screen reveals PP targets that enhance oncolytic VSVΔ51. (**A**) Schematic diagram representing the workflow of the high-throughput screen. (**B**–**E**) Human 786-0 cells were seeded in 96-well plates, transfected with RNA from the MISSION® silencing RNA (siRNA) Human Phosphatase Library or corresponding controls for 48 h. Cells were then infected with VSVΔ51 tagged with firefly luciferase (VSVΔ51-fluc) at a multiplicity of infection of 0.05. Blue dots indicate cell treated with vanadate. Red dots indicated cells transfected with RIG-I siRNA. Green dots indicate cells transfected with scramble siRNA. (**B**) Oncolysis enhancing factor was calculated as described in the methods and plotted. Candidates of interest are labeled as shown. (**C**) Supernatant was assessed for viral titer by high-throughput titration 48hpi and expressed a fold-change over infected-only cells, and by significance from average infectivity of infected-only cells by unpaired t-test assuming unequal variance. (**D**) Oncolysis enhancing factor of candidates were plotted against fold-change viral titer. Top candidates of interest are labeled as shown.

Supplemental Table S2), 786-0 cells transfected with ACP2 siRNA and infected with VSVΔ51 were probed by real-time quantitative polymerase chain reaction (qPCR) for ACP2 RNA transcripts. Indeed, we confirmed that the siRNA reduced ACP2 transcription both in the presence and absence of infection (Fig. 2B). To confirm this at the protein level, lysates were probed for ACP2 protein by immunoblotting which also confirmed knockdown of ACP2 (Fig. 2C).

Given the successful knockdown using our ACP2 siRNA, we quantified the increase in VSVΔ51 viral titer using standard plaque assay (Fig. 2D). Moreover, we demonstrated its ability to increase tagged VSVd51-GFP expression by florescence microscopy (Fig. 2E) and VSV-M RNA expression by qPCR, both indicating increased VSVΔ51 viral titer (Fig. 2F). To evaluate cell viability, resazurin metabolic dye was used and showed that knockdown of ACP2 increased the oncolytic activity of VSVΔ51, akin to the results of the screen. Transfection with ACP2 siRNA alone did not significantly decrease viability; however, the further addition of VSVΔ51 significantly reduced viability to 60% 72 h post-infection compared to 80% with virus alone (Fig. 2G). Together, these results confirm ACP2 as a suitable target of interest to enhance oncolytic VSVΔ51.

Regulation of the type I interferon response by ACP2

Asides from roles in neurodevelopment in mice[19,20], ACP2 was mainly established to be instrumental in lysosomal activity for the processing of cellular degradation products[21,22]. There are previous reports suggesting a role for ACP2 in regulating herpes-simplex virus (HSV) cellular entry[23], but none directly describing its role in regulating the antiviral defense response. Therefore, to investigate this potential new role for ACP2, we performed in silico analysis via RNA sequencing. RNA from 786-0 cells transfected with siRNA against ACP2 was extracted after 24 h of infection with VSVΔ51, then sequenced for whole transcriptome changes and gene expression profiles calculated between experimental conditions. Between uninfected cells transfected with scramble siRNA or siRNA against ACP2, 1,080 genes were significantly upregulated ($P < 0.05$, $\log_2$-fold change > 1) and 1,813 genes were significantly downregulated (Fig. 3A). Analysis of involved gene ontology (GO) terms using the GOrilla tool revealed significant downregulation of antiviral-related terms including "type I interferon signaling pathway" and "defense response to virus"[24,25] (Fig. 3B). A heatmap with differential expression of all genes

Target	FC viral titer	Oncolysis enhancing factor	Gene ID	Gene name	Accession #
PTP1C2	1.62	0.54	ACP2	Acid phosphatase 2, lysosomal	NM_001610
PTP2C2	2.21	1.31	ACP2	Acid phosphatase 2, lysosomal	NM_001610
PTP3D2	1.88	0.69	ACP5	Acid phosphatase 5, tartrate resistant	NM_001111034
PTP1C3	2.22	1.31	ACYP1	Acylphosphatase 1, erythrocyte (common) type	NM_203488
PTP2D5	2.07	1.34	CTDP1	CTD (carboxy-terminal domain, RNA polymerase II, polypeptide A) phosphatase, subunit 1	NM_004715
PTP2E5	2.09	0.79	CTDSP1	CTD (carboxy-terminal domain, RNA polymerase II, polypeptide A) small phosphatase 1	NM_021198
PTP2D8	1.71	0.71	DUSP26	Dual specificity phosphatase 26 (putative)	NM_024025
PTP3A9	1.89	0.98	DUSP6	Dual specificity phosphatase 6	NM_001946
PTP3E10	1.87	0.62	ENPP7	Ectonucleotide pyrophosphatase/phosphodiesterase 7	NM_178543
PTP13G3	2.30	0.50	ENTPD2	Ectonucleoside triphosphate diphosphohydrolase 2	NM_203468
PTP1F11	2.13	1.09	EYA2	Eyes absent homolog 2 (Drosophila)	NM_005244
PTP3F11	1.87	0.47	EYA2	Eyes absent homolog 2 (Drosophila)	NM_005244
PTP6H2	1.61	1.48	G6PC3	Glucose 6 phosphatase, catalytic, 3	NM_138387
PTP4D3	2.24	0.56	ILKAP	Integrin-linked kinase-associated serine/threonine phosphatase	NM_176799
PTP6E4	1.75	0.45	INPP5E	Inositol polyphosphate-5-phosphatase, 72 kDa	NM_019892
PTP6F5	2.36	0.56	LHPP	Phospholysine phosphohistidine inorganic pyrophosphate phosphatase	NM_022126
PTP4D9	2.51	1.14	PFKFB2	6-phosphofructo-2-kinase/fructose-2,6-biphosphatase 2	NM_001018053
PTP4H9	1.63	0.85	PGAM4	Phosphoglycerate mutase family member 4	XM_930828
PTP4D10	1.85	0.50	PHOSPHO2	Phosphatase, orphan 2	NM_001008489
PTP6F11	2.45	1.02	PPAPDC3	Phosphatidic acid phosphatase type 2 domain containing 3	NM_032728
PTP8H2	2.35	1.64	PPM1B	Protein phosphatase, Mg2+/Mn2 + dependent, 1B	NM_001033556
PTP9D4	2.68	1.66	PPM1M	Protein phosphatase, Mg2+/Mn2 + dependent, 1 M	NM_144641
PTP9B5	2.19	1.17	PPP1R10	Protein phosphatase 1, regulatory subunit 10	NM_002714
PTP9C6	1.64	0.45	PPP1R14A	Protein phosphatase 1, regulatory (inhibitor) subunit 14 A	NM_033256
PTP7A7	3.00	1.60	PPP1R16A	Protein phosphatase 1, regulatory subunit 16 A	NM_032902
PTP9D9	2.25	0.60	PPP2R2C	Protein phosphatase 2, regulatory subunit B, gamma	NM_020416
PTP7H10	2.66	1.45	PPP4C	Protein phosphatase 4, catalytic subunit	NM_002720
PTP7B11	2.88	1.38	PPP4R1	Protein phosphatase 4, regulatory subunit 1	NM_005134
PTP9C11	2.03	0.81	PPP4R1L	Protein phosphatase 4, regulatory subunit 1-like	NM_018498
PTP12D2	2.92	1.57	PSPH	Phosphoserine phosphatase	NM_004577
PTP12F2	2.42	0.82	PTER	Phosphotriesterase related	NM_001001484
PTP14B8	2.00	0.61	PTPN20A	Protein tyrosine phosphatase, non-receptor type 20 A	XM_931711
PTP10E6	1.70	0.91	PTPN6	Protein tyrosine phosphatase, non-receptor type 6	NM_002831
PTP12F8	2.95	0.46	PTPN7	Protein tyrosine phosphatase, non-receptor type 7	NM_002832
PTP16F4	2.86	0.74	PTPRO	Protein tyrosine phosphatase, receptor type, O	NM_030668
PTP10G10	2.13	1.85	SSH3	Slingshot homolog 3 (Drosophila)	NM_018276
PTP12H10	2.80	1.29	SSU72	SSU72 RNA polymerase II CTD phosphatase homolog (S. cerevisiae)	NM_014188
PTP12H11	2.89	1.25	THTPA	Thiamine triphosphatase	NR_023314

Table 1. Top hits from the high-throughput siRNA phosphatase screen. *FC* Fold-change.

related to the "type I signaling pathway" GO term was plotted which overall demonstrates repression of related genes upon transfection with siACP2, in both the absence and presence of VSVΔ51 infection (Fig. 3C, S3).

Furthermore, we analyzed downregulated gene lists using the Kyoto Encyclopedia of Genes and Genomes (KEGG) pathways to identify relevant cellular processes. We found that ACP2 knockdown by siRNA affected pathways including the lysosome pathway and the RIG-I-like receptor signaling pathway (Fig. 3D). The former hit validates our knockdown method given that ACP2 is known to be responsible for regulating lysosomal pathways[22], while the latter further implicates innate antiviral immunity to be a new repressed pathway upon ACP2 knockdown (Fig. S4). Given that our in silico analyses support the repression of IFN-1 pathways, we wanted to confirm the suppression of IFN-1 effectors by ACP2 knockdown. Indeed, quantification of mRNA 24 h after infection showed that transfection with siRNA against ACP2 significantly reduced transcription of the antiviral IFN-1 effectors, MX2 and IFITM1 (Fig. 3E).

VSVΔ51 expressing shACP2 has increased viral infectivity in human tumor models

The second objective of this study was to test the feasibility of cloning RNAi into a VSVΔ51 vector against a PP target for improved infectivity. The cloning plan for the viral backbone is outlined in Fig. 4A. After generating a pre-miR-30 short hairpin cassette with our predetermined siRNA sequence against ACP2 flanked by XhoI

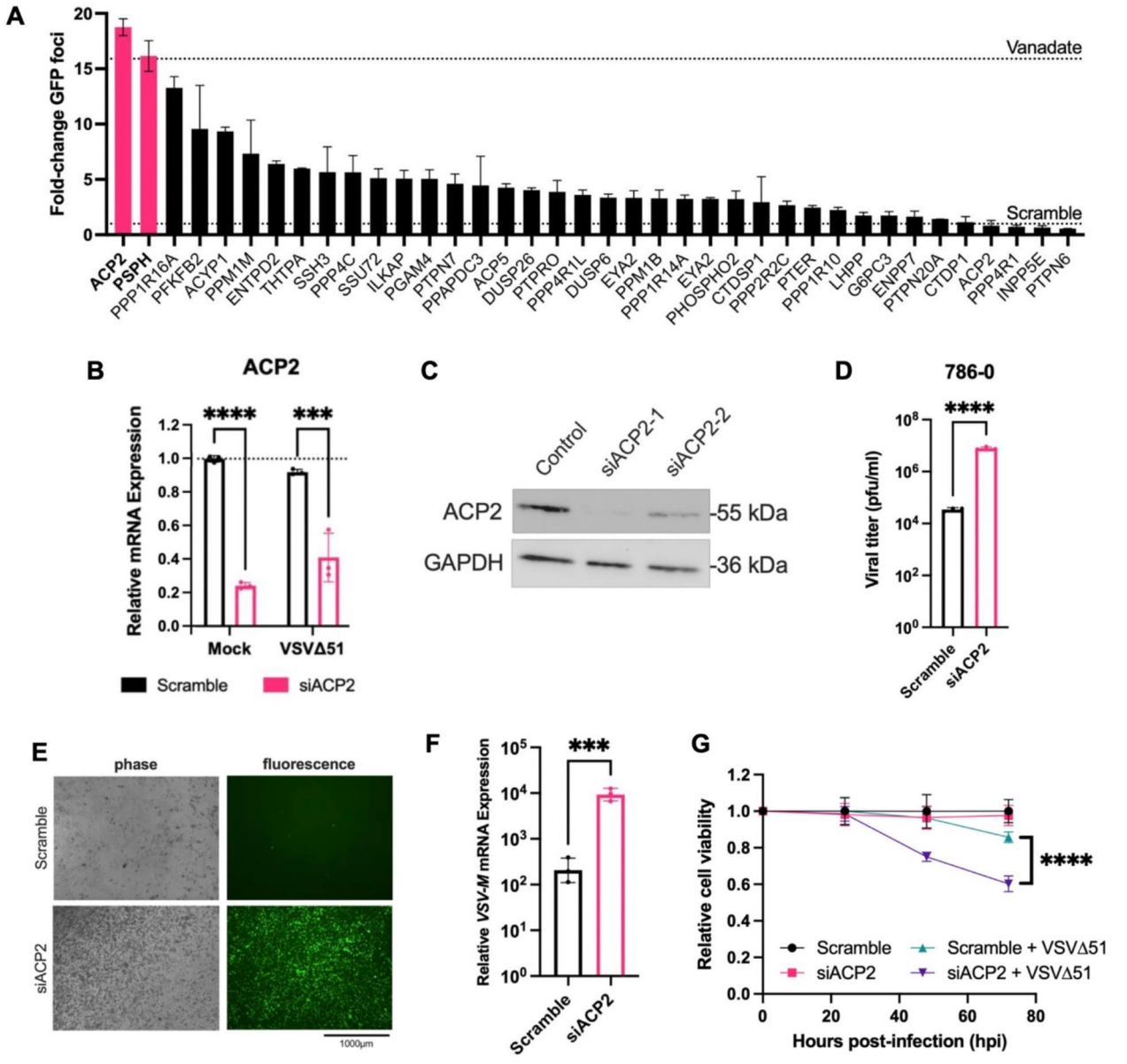

Fig. 2. ACP2 knockdown increases VSVΔ51 infectivity and oncolysis. (**A**) Top hits from the high-throughput screen were validated in 786-0 cells using a similar protocol. Cells were transfected with PP-targeting siRNA for 48 h, then infected with VSVΔ51 tagged with green fluorescent protein (VSVΔ51-GFP) at a multiplicity of infection of 0.05. Fluorescent foci were counted 24 h post infection (hpi) and expressed as fold-change over the infected-only condition ($n = 3$, mean). (**B**–**F**) 786-0 cells were transfected with siRNA targeting ACP2 for 6 h, then the media was replaced. 48 h later, cells were infected with VSVΔ51-GFP (MOI 0.01). (**B**) Cells were lysed 24hpi for RNA extraction and analyzed for ACP2 transcripts by qPCR ($n = 3$, mean ± SD; $^{***}P < 0.001$, $^{****}P < 0.0001$ by two-way ANOVA). (**C**) Cellular lysates were probed for ACP2 and GAPDH protein by immunoblotting. Representative blots are shown. (**D**) Supernatant was taken 24hpi and analyzed for viral titer by plaque assay ($n = 3$, mean ± SD; $^{****}P < 0.0001$ by unpaired t-test). (**E**) Representative fluorescent images were taken 24hpi. (**F**) Infected cells were lysed 24hpi for RNA extraction and analyzed for VSV-M transcripts by qPCR ($n = 3$, mean ± SD; $^{***}P < 0.001$ by unpaired t-test). (**G**) Relative viability was measured by resazurin metabolic dye over mock transfected, uninfected controls at indicated timepoints ($n = 3$, mean ± SD; $^{****}P < 0.0001$ by two-way ANOVA).

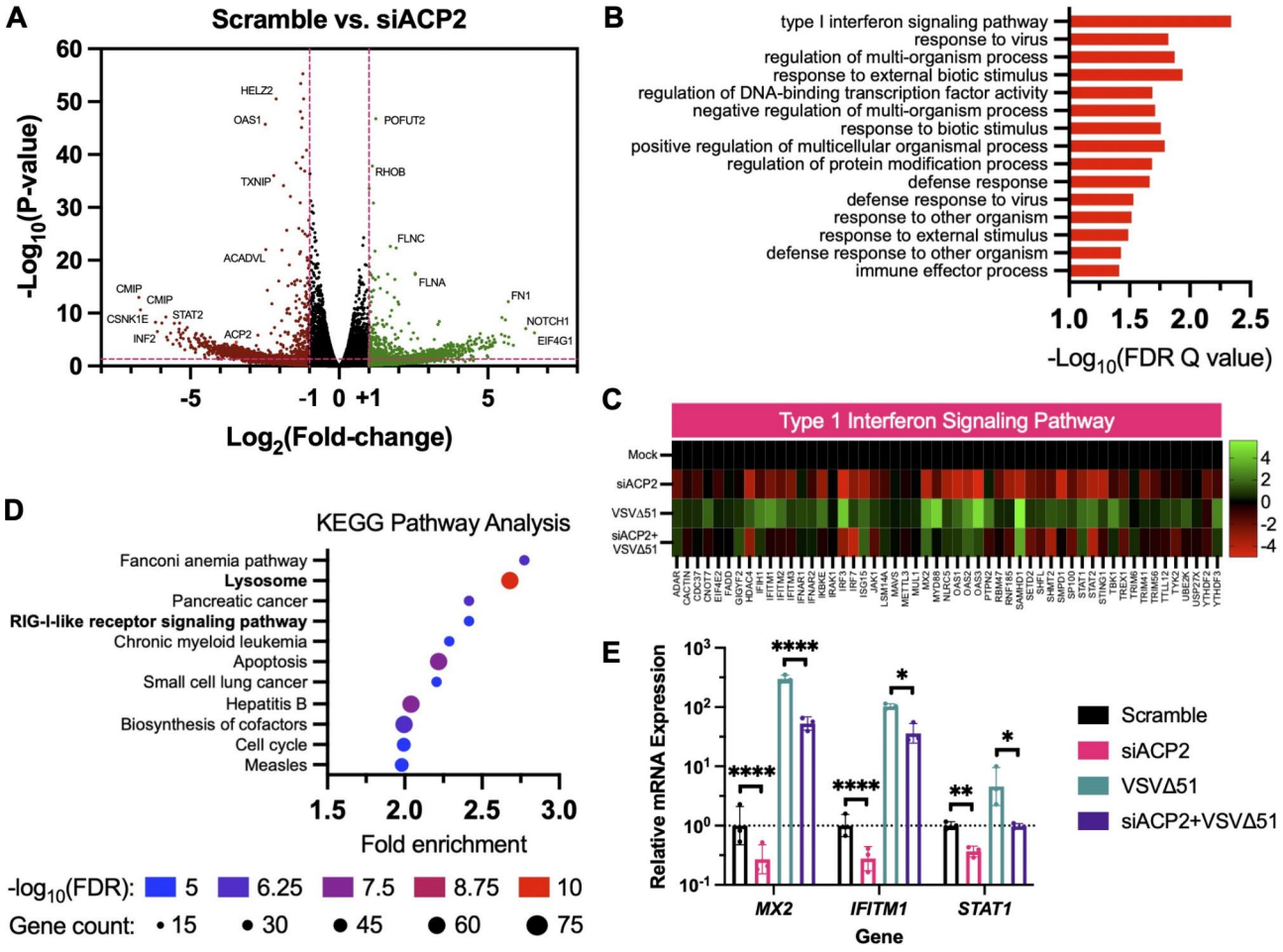

Fig. 3. ACP2 is involved in the IFN-1 response. (**A**–**D**) 786-0 cells were transfected with siRNA targeting ACP2 for 6 hours, then the media was replaced. 48 hours later, cells were infected with VSVΔ51-GFP (MOI 0.01). RNA was then extracted 24 hours post infection (hpi) and sequenced in two biological replicates. Processing by KALLISTO pseudo-alignment and SLEUTH yielded normalized log2-fold change in differential gene expression and P-values. (**A**) Each gene was plotted for fold-change and P-value in a volcano plot, notable hits were labeled. (**B**) Significantly downregulated (> 1 log2-fold change) gene expressions were processed by Gorilla to identify relevant gene ontology (GO) terms. FDR = False Discovery Rate. (**C**) A heatmap of the fold-change expression of gene related to the "Type 1 Interferon Signaling Pathway" GO term was plotted. (**D**) Significantly downregulated genes were input into the Graphite and CliPPER tools to determine relevant Kyoto Encyclopedia of Genes and Genomes (KEGG) pathways. (**E**) 786-0 cells were transfected with siRNA targeted ACP2, then infected with VSVΔ51 (MOI 0.05). Cells were lysed 24 h later and RNA was extracted. MX2 and IFITM1 mRNA transcripts were quantified by qPCR ($n = 3$, mean ± SD; $^{*}P < 0.05$, $^{***}P < 0.001$ by two-way ANOVA).

and NheI restriction, we digested the oligonucleotide sequence into a VSVΔ51 plasmid between the G and L proteins.

To confirm the knockdown efficacy of the resulting bioengineered virus, we infected 786-0 cells with either VSVΔ51 against non-targeting control (VSVΔ51-NTC) or shACP2 (VSVΔ51-shACP2) and analyzed their lysate for miR-30 expression and ACP2 mRNA. Indeed, our analysis by qPCR with primers against miR-shACP2 found increased expression by VSVΔ51-shACP2 at both multiplicities of infection (MOI) 0.01 and 0.1 as soon as 12 h after infection (Fig. 4B). Moreover, our data found about 30% repression of ACP2 transcription in cells infected with VSVΔ51-shACP2 (Fig. 4C) relative to the control. These data confirm proper expression of our desired miR-30 cassette and effective knockdown of our target gene, ACP2, in infected cells. To indirectly support that the mechanism of viral enhancement remained through IFN-1, we found no significant difference in viral titer between VSVΔ51-shACP2 relative to the control in IFN-1 deficient Vero cells (Fig. S6).

After establishing the functionality of VSVΔ51-shACP2, we wanted to test its efficacy in increasing viral infectivity. Upon infection of 786-0 cells with VSVd51-shACP2 or VSVd51-NTC at different MOI, resulting titers showed significant increases with VSVΔ51-shACP2 at higher MOI, supporting increased viral output per infected cell (Fig. 4D). In testing the growth kinetics of VSVΔ51-shACP2, we found that VSVΔ51-shACP2 was able to enhance viral output in both the single- and multistep growth curves performed in 786-0 cells

which suggest that VSVΔ51-shACP2 exhibits increased viral spread and replication over the control (Fig. 4E). To confirm that our novel bioengineered virus has increased infectivity across multiple tumor contexts, we tested both VSVΔ51-NTC and VSVΔ51-shACP2 in several cell lines. Indeed, we found that VSVΔ51-shACP2 had greater viral titers after 24 h of infection in human in vitro models of lung, breast, and sarcoma tumors (Fig. 4F). VSVΔ51-shACP2 also showed increased cytotoxicity relative to the control across all tested cell lines at the same MOI (Fig. 4G).

Finally, to confirm the proposed mechanism of action of IFN-1 repression by our novel VSVΔ51-shACP2, we analyzed 786-0 cell lysates infected for 24 h with VSVΔ51-shACP2 for IFN-1 effectors, MX2 and IFITM1. While the magnitude was not large, VSVΔ51-shACP2 was still able to show significant repression of MX2 and IFITM1 transcription (Fig. 4H), similar to what was observed in 3E with the silencing RNA against ACP2. Interestingly, similar to what has been previously observed vanadium-based pan-phosphatase inhibitor compounds, IFN-β mRNA levels were not affected suggesting that ACP2 may preferentially intercept late-phase IFN-1 response pathways (Fig. S7). To further demonstrate that this phenomenon was not specific to the 786-0 model, we found similar results when we performed the same experiment in the human HT-1080 fibrosarcoma cells (Fig. S8). Taken altogether, this data supports that VSVΔ51-shACP2 has more potent infectivity and cytotoxicity in tumor cells compared to the control VSVΔ51 vector and operates via repression of the IFN-1 axis.

Discussion

Here, we demonstrate that multiple PPs have intimate roles in regulating the antiviral response through a high-throughput screening approach. Knockdown of some PP transcripts confer enhanced VSVΔ51 infectivity and/or oncolysis. Further molecular analysis of our top hit, ACP2, confirmed its VSVΔ51 enhancing activity and found that its mechanism of action hinges upon repression of IFN-1 signaling and its downstream antiviral effectors. We then secondarily demonstrated that upon cloning of an ACP2-targeting shRNA into a VSVΔ51 backbone, the resulting VSVΔ51-shACP2 virus exhibited increased infectivity and cytotoxicity over its non-targeting control counterpart in multiple cancer cell lines.

Balance of the protein phosphatome is crucial to the regulation of innate cellular processes including the antiviral response. The targeting of kinases using small molecular inhibitors to favor dephosphorylated states has been shown to influence interferon signalling and resistance to infection in a multitude of ways. For example, in light of the recent SARS-CoV-2 (COVID-19) pandemic, high-specificity kinase inhibitors have been explored as a clinical therapeutic to repress SARS-CoV-2 infection[26]. On the other hand, phosphatases are much harder to target with specificity given that (1) a highly conserved active site or phosphatase binding pocket makes specificity difficult, and (2) the positively charged active site challenges cell membrane permeability[27,28]. For these reasons, it is more feasible to execute specific PP inhibition via gene knockdown using RNAi as opposed to using small molecules[16]. Accordingly, we applied this strategy with our HTS using the MISSION® silencing RNA (siRNA) Human Phosphatase Library to identify relevant PP targets to enhancing OV infectivity.

Aside from ACP2, our HTS yielded some interesting insights into the roles of other PPs that simultaneously enhanced VSVΔ51 infectivity and oncolysis (Table 1). Eyes absent (EYA) proteins are haloacid dehalogenase PPs that have been implicated to interact with signal transducers of innate antiviral immunity including MAVS, STING and NLRX1. Transduction of EYA1-4 into murine embryonic fibroblasts has been reported to show increased IFN-β and pro-inflammatory CXCL10 production when stimulated with pattern-associated molecular patterns[29]. In our HTS, knockdown of both EYA2 and EYA4 significantly increased VSVΔ51 viral titers (Fig. 1D). Secondly, we found that knockdown of both regulatory and catalytic subunits of the phosphoprotein phosphatases family (PP1R16A, PPP4R1, PPP4C, PPP1R10, PPP1R14A, PPP4R1L, and PPP2R2C) conferred VSVΔ51 enhancing activity. Phosphoprotein phosphatases such as PP1 and PP2A have been shown to inactivate interferon response factors (IRF) to ultimately impede IFN responses in response to viral infection[30–32]. In the case of PP1, the target PPP1R14A is responsible for negative control of the PP1 catalytic subunit; therefore, its knockdown allows for dysregulated PP1 activity and impedance of the IFN response to ultimately allow for increased viral infection[33].

On the other hand, some identified hits run counterintuitive to literature. PPP4C and PPP4R1, the two dimeric components of PP4, were part of the short list of 38 hits we identified to simultaneously increase VSVΔ51 infectivity and oncolysis upon genetic knockdown (Table 1). However, PP4 activity has been implicated to dephosphorylate and deactivate TBK1 to disrupt IFN-1 production via IRF3 repression. The same study found that knockdown of PPP4C in macrophages increased IFN-β production and thus reduced VSV replication[34]. This discordance therefore raises two assertions: (1) the need for validation of these hits to remove false positives, or (2) the elucidation of different roles of the same PP across different contexts (e.g., in immune vs. tumor cells). In both scenarios, further investigation is warranted to cement the role of each respective PP in the IFN pathway and further our understanding of how the phosphatome interacts with the natural anti-viral response.

Nonetheless, in this study we were successful in identifying the role of ACP2 in the innate antiviral response. Given the roles of ACP2 in regulating lysosome and endosome trafficking, knockout of ACP2 was previously shown to compromise influenza A virus membrane fusion, thereby halting viral entry[23]. In the context of VSVΔ51, it appears that ACP2 knockdown is not involved in VSV trafficking[35], but rather ACP2 may be necessary for intracellular viral detection given the identification of repression of the "RIG-I-like receptor signalling pathway" KEGG pathway term on in silico analysis (Fig. 3D, S3, S4). One working hypothesis for this interference may depend on the required localization of toll-like receptors (TLR) to endosomes during viral detection, which may be compromised without functional ACP2[36]. A secondary explanation could involve compromise of the JAK-STAT signalling pathway, whose components, like STAT2, were shown to be downregulated upon ACP2 knockdown from our transcriptome analysis (Fig. 3C). Interference of signal transduction following IFN-β binding could potentially explain our observed decreases in downstream antiviral effectors such as *MX2* and

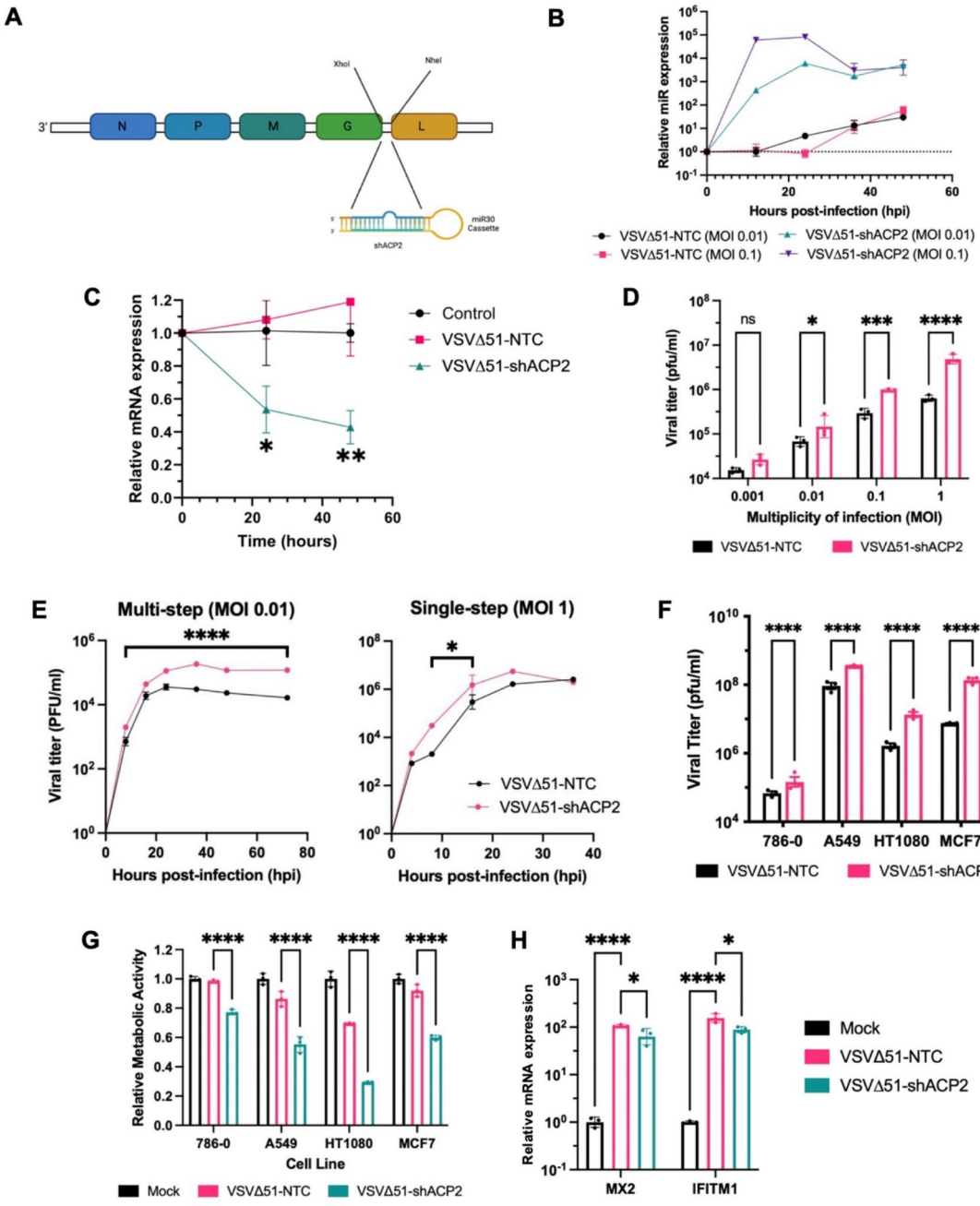

IFITM1 (Fig. 3E). It is important to note that while our data supports a link between ACP2 and IFN-1 responses (Fig. S6), next steps may involve formally investigating their dependency through knockout models.

The design of our RNAi-expressing VSVΔ51 vector (Fig. 4A) is based upon previous studies establishing the utility of a miR-30 promoter for the expression of shRNA[37]. The resulting VSVΔ51-shACP2 primarily represents a proof-of-concept that PPs can be targeted using RNAi expressed by an OV vector for beneficial effects. Indeed, our VSVΔ51-shACP2 demonstrates improved viral infectivity and oncolysis through its predicted mechanism of action of IFN-1 repression (Fig. 4). However, there remain several limitations to this approach before it can be considered for therapeutic use. Firstly, while our knockdown efficacy was significant, it was only capable of modestly reducing ACP2 transcripts by less than 2-fold, compared to 10-fold using direct siRNA transfection. This translated to weaker inhibition of downstream IFN-1 effectors (Fig. 4H). Given that levels of IFN-β are not affected by siACP2 or VSVΔ51-shACP2 infection (Fig. S7), it is possible that the kinetics of IFN-β-mediated

◀**Fig. 4**. VSV expressing shRNA against ACP2 has improved infectivity and oncolysis. (**A**) Schematic detailing the viral backbone of VSVΔ51-shACP2. (**B**–**D**) 786-0 cells were infected with either VSVΔ51-non targeting control (NTC) or VSVΔ51-shACP2 (with indicated multiplicity of infection, MOI). (**B**) Cells were lysed, miRNA was extracted at indicated timepoints, then probed for miR-30 and shRNA against ACP2 cassette expression. (**C**) Lysates were extracted from cells 24 and 48 hpi and RNA was extracted. *ACP2* mRNA transcript levels were probed by qPCR ($n=3$, mean ± SD; $^{*}P<0.05$, $^{**}P<0.01$ by one-way ANOVA). (**D**) Supernatant of infected cells with different MOI were assessed for VSVΔ51 viral titer 24 hpi by viral plaque assay ($n=3$, mean ± SD; $^{*}P<0.05$, $^{***}P<0.001$, $^{****}P<0.0001$ by two-way ANOVA). (**E**) Multi-step and single-step growth curves of 786-0 infected with VSVΔ51-NTC or VSVΔ51-shACP2 (MOI 0.01 or 1). Supernatants were quantified by viral plaque assay at specified timepoints ($n=3$, mean ± SD; $^{*}P<0.05$, $^{****}P<0.0001$ by Student's t-test at each time point analyzed independently. (**F**–**G**) Various cell lines were infected with VSVΔ51-NTC or VSVΔ51-shACP2 (MOI 0.01). (**F**) Supernatant was analyzed for VSVΔ51 viral titer 24 hpi by viral plaque assay ($n=3$, mean ± SD; $^{****}P<0.0001$ by two-way ANOVA). (**G**) Cell viability was measured by resazurin metabolic dye 48 hpi, normalized to the uninfected condition ($n=3$, mean ± SD; $^{****}P<0.0001$ by two-way ANOVA). (**H**) RNA was extracted from 786-0 cells infected with VSVΔ51-NTC or VSVΔ51-shACP2 24 hpi, then probed for *MX2* and *IFITM1* mRNA transcripts by qPCR ($n=3$, mean ± SD; $^{*}P<0.05$, $^{****}P<0.0001$ by one-way ANOVA).

resistance overtake ACP2 silencing when provided from within the virus, leading to decreased viral uptake and knockdown efficiency. Another important consideration is that upon infection of healthy tissues, the off-target gene silencing does not compromise the safety profile of the virus. Strategies like placing RNAi effectors under tissue-specific promoters could help mitigate unwanted gene knockdown events. Finally, the immediate clinical utility of VSV is limited given lack of experience in human clinical trials; therefore, exploration of the relationship between PP knockdown and its ability to potentiate other viral vectors further along in clinical trial pipelines (i.e., *HSV-1*) represent intriguing avenues of investigation. Comprehensive strategies on addressing each of these limitations: efficacy, safety, and vector selection are outlined in a related review by our group[16].

The development of innovative strategies to improve efficacy are paramount for the continued success of oncolytic virotherapy. Altogether, this study represents a proof-of-concept for incorporating RNAi targeting PPs for increased viral infectivity and oncolysis. Next steps for this experimental series would be to validate and clone several other PP targets into VSV and test their impact on OV infectivity and oncolysis. If multiple successful candidates are identified, testing different combinations for synergistic viral enhancing or oncolysis represents an intriguing avenue of investigation. Casting a wider net could pave the way for unexpected therapeutic synergies and hopefully, a better chance at clinical impact by OVs.

Materials and methods

Study design

In this controlled laboratory study, the hypothesis was initially formulated upon the previous observation that vanadium-based compounds, which operate as pan-phosphatase (PP) inhibitors, increases VSVΔ51 infectivity and oncolysis. Subsequently, the objective was to identify PPs that could mimic this oncolytic virus enhancing effect. An in vitro approach was taken by employing a high throughput screen using the MISSION® siRNA Human Phosphatase Library to identify PP targets, that when knocked down, could confer OV enhancement. Upon identification of top candidates, subsequent hypotheses led us to investigate their mechanism of action and its potential exploitation for further therapeutic gain.

Drugs and chemical reagents

Sodium orthovanadate (vanadate, Na_3VO_4), the main vanadium-based compound used in the study, was obtained from Sigma-Aldrich (cat. 450243). To prepare the sodium orthovanadate, the compounds was dissolved in water, pH-adjusted to 10, boiled until translucent, then allowed to cool to room temperature to ensure formation of stable monomeric vanadate[38]. The remainder of drugs, chemicals, and cytokines along with their supplies, catalog numbers and solvent are listed in Supplemental Table S1.

Cell lines

A complete list of the cell lines (species, tissue type, supplier) can be found in Table S1. Cells were maintained in Dulbecco's modified Eagle's medium (DMEM; HyClone cat.10–013) supplemented with 1% (v/v) penicillin-streptomycin (Gibco), 30mM HEPES buffer, and 10% (v/v) serum composed of 3-parts HyClone newborn calf serum (Thermo Fisher, cat. SH3011803) and 1-part Fetal Bovine Serum (Gibco, cat. 12483020). Cells were incubated at 37 °C and 5% CO_2 conditions in a humidified incubator. Phase and fluorescence images were taken using the EVOS Live Cell Imaging System (Thermo Fisher).

Oncolytic viruses

The Indiana serotype of vesicular stomatitis virus harboring a deletion of methionine 51 in the M protein (VSVΔ51) and insertion of green fluorescence protein (GFP) or firefly luciferase (FLuc) were used throughout this study[39]. All viruses were propagated on Vero cells and purified on 5–50% OptiPrep (Sigma-Aldrich, St. Louis, MO) gradients. Viral titers were determined by high-throughput titration according to published protocol[17], or standard plaque assay on Vero cells according to published protocol[40].

The oncolytic VSVΔ51 virus backbone and propagation protocols have been previously described[39]. In short, we assessed 3 individual siRNAs from the ON-TARGETplus Non-targeting Control Pool (D-001810-

01,D-001810-02, and D-001810-03) and siACP2 targeting ACP2 purchased from Dharmacon. The siRNAs each met the threshold of at least three mismatches to all human, mouse and rat transcripts in the current RefSeq database. We resuspended siRNAs in siRNA Buffer (5X siRNA Buffer, Dharmacon) to generate 20 µM stocks. For transfection, 5 µL of Lipofectamine™ RNAiMAX Transfection Reagent (Thermo Fisher Scientific) was combined with 250 µL Opti-MEM and incubated for 5 min. The RNAiMAX complex was then combined with siRNAs diluted in Opti-MEM (2 µL of siRNA with 250 µL of Opti-MEM). The siRNA-RNAiMAX complex was then incubated for 20 min at room temperature and added in a gentle dropwise fashion to wells with 5E5 cells HEK293T cells suspended in 1.5 mL of media with serum. 24 h post-transfection, designated wells were infected with VSVΔ51-GFP for 30 min. The siRNA treatments did not sensitize to virus infection. We ordered oligos (Table S3) for insertion into the modified miR-30 cassette with the selected NTC and siACP2 sequence within the VSVΔ51 backbone.

To generate replication-competent shRNA-expressing VSVΔ51 viruses, a non-targeting control (NTC) (Table S3) or a siRNA targeting ACP2, incorporated in a pre-miR-30-based short hairpin cassette flanked by XhoI and NheI restriction sites, were obtained from Integrated DNA Technology (IDT). The VSVΔ51 plasmid was cleaved with XhoI and NheI (NEB), and the shRNA inserts were ligated individually into the VSVΔ51 empty vector at the gene junction between the G and L proteins, following established protocols. Sanger sequencing (performed at StemCore Laboratories, Ottawa, ON) was conducted to confirm the constructs' integrity. The viruses were generated using an infection-transfection method, as previously described[37].

High throughput siRNA screen

The entire experimental workflow is graphically summarized as Fig. 1A. The phosphatase library used for the high-throughput screen was taken from the MISSION® siRNA Human Phosphatase Library (cat. SI03200) targeting 303 phosphatase genes (1131 siRNA total) was acquired from Millipore Sigma and reconstituted by diluting in molecular grade RNase, DNase, protease-free water (Sigma, cat. W4502) to a final stock concentration of 2.5µM and stored at -20 °C until use. Immediately prior to transfection, a working plate was derived from each library plate by diluting phosphatase siRNA (siPP) in molecular grade water to a working concentration of 0.2µM. Human 786-0 renal cell carcinoma cells were seeded at a final cell density of 1.6×10^4 cells/well in 96-well microplates and transfected with siRNA using Lipofectamine® RNAiMax (Invitrogen, cat. 13778150). RNAiMax Lipofectamine was first prepared by mixing into serum-free Opti-MEM I Medium (Thermo Fisher Scientific, cat. 31985070) and allowed to incubate for 5 min. Respective siRNAs were then diluted into this solution and incubated for 20 min to allow for formation of siRNA-lipid complexes, then mixed into the cell suspension at a final siRNA concentration of 20nM. All dilutions were performed using the BioTek™ Precision™ Microplate Pipetting System (Thermo Fisher Scientific) and solutions were dispensed using the MicroFlo Select™ Microplate Dispenser (Biotek™). After 48 h incubation in standard conditions, cells were subsequently infected with VSVΔ51-GFP or FLuc (MOI 0.05) using the manual Liquidator 96 Pipetting System (Mettler Toledo).

For fluorescent foci counting, GFP-fluorescence units were obtained using a Cellomics Arrayscan VTI HCS Reader after 24 h. For luminescence-based tittering, infectious viral particles were quantified by high-throughput titration 48 h post infection (hpi) and relative metabolic activity assessed by resazurin metabolic dye (Millipore Sigma, cat. SI03200). The dye was added to samples at a 1:10 dilution and incubated for 2 h. Using a BioTek Microplate Reader (Norgen BioTek Corp, Ontario, Canada) and Gen5 2.07 software, fluorescence was measured at 590 nm upon excitation at 530 nm. Readings were normalized to the average of the uninfected, mock treated condition. To calculate *oncolysis enhancing factor* (formerly *viral sensitizing factor*[41]) for ranking of primary hits based on viability, the following equation was used.

$$Oncolysis\ enhancing\ factor = Log_{10}\left(\frac{Viability\ siPP\ alone}{Viability\ siPP + VSV\Delta 51}\right)$$

Each microplate, performed in triplicate, consisted of 80 wells of tested siRNA, two scramble siRNA controls (Mission® siRNA Universal Negative Control #1, Sigma, cat. SIC001), two vanadate-treated wells (125µM) and two RIG-I (Millipore Sigma, cat. NM_014314, siRNA ID SASI_Hs01_00047980) knockdowns acting as transfection controls. This plate layout is graphically represented as Figure S1B.

Small-interfering RNA (siRNA) transfection

786-0 cells were seeded at 40% density in 24-well plates in serum-free DMEM overnight. Transfections were performed using control, scramble RNA (ON-TARGETplus Non-targeting Control Pool, #D-001810-10-05, Horizon Discovery), custom siRNA against lysosomal acid phosphatase 2 (ACP2) (Thermo Fisher). Custom siRNA sequences are listed in Table S2. Transfection was performed using Lipofectamine™ RNAiMAX Transfection Reagent (Thermo Fisher, cat. 13778075) according to manufacturer's protocol in Opti-MEM™ I Reduced Serum Medium (Thermo Fisher, cat. 31985062). After 6 h, media containing siRNA was replaced with DMEM supplemented with 1% (v/v) penicillin-streptomycin (Gibco), 30mM HEPES buffer and 10% (v/v) serum composed of 3-parts HyClone newborn calf serum (Thermo Fisher, cat. SH3011803) and 1-part Fetal Bovine Serum (Gibco, cat. 12483020). Upon reaching approximately 80% confluency, cells were treated with reagents or infected with VSVΔ51 as specified.

Quantitative real-time polymerase chain reaction

To first homogenize cells for RNA yield, cells were lysed using the QIAshredder (Qiagen, cat. 79656). RNA was then extracted using the QIAGEN RNeasy kit (Qiagen, cat. 74106) according to manufacturer's protocol and quantified using a NanoDrop™ One Microvolume UV-Vis Spectrophotometer (Thermo Fisher Scientific, Rockford, IL). The RevertAid H-Minus First Strand cDNA Synthesis Kit (Thermo Fisher, cat. K1632) was used

to generate corresponding cDNA from extracted RNA. To isolate miRNA, RNA extractions were performed using TRIzol™ reagent as per manufacturer protocol (Invitrogen). The miRNA 1st-Strand cDNA Synthesis Kit was used according to manufacturer protocol (Agilent, cat. 600036).

Resulting nucleic acid was subject to quantitative real-time PCR using primers outlined in Table S2, Applied Biosystems PowerUp SYBR Green Master Mix (Thermo Fisher, cat. A25776) in a 7500 Fast Real-Time PCR system (Applied Biosystems, Foster City, CA). Gene expression was calculated using the Pfaffl method[42]. For miRNA qPCR, the universal poly-A tail (Agilent) was used as the reverse primer.

RNA-sequencing analysis

RNA was extracted from cell lysates as described in the previous section. Upon quantification and quality assurance, samples were shipped to the Donnelly Sequencing Centre (University of Toronto) and mRNA-seq libraries were generated using the NEB NEBNext Ultra II Directional RNA library prep kit according to manufacturer's protocol. Libraries were sequenced using the Illumina NovaSeq with paired-end 150 bp reads. After sequencing, resulting Fastq files were checked for quality using FastQC (Babraham Bioinformatics, United Kingdom). Pseudo alignment and transcript quantification were performed with KALLISTO[43], and differential expression was determined using SLEUTH[44]. Gene ontology analysis was performed using the Gene Ontology enrichment analysis and visualization tool (GOrilla)[24,25]. Signaling pathway topology analyses were performed using Graphite and CliPPER (Department of Biology, University of Padova, Italy)[45,46]. Finally, Kyoto Encyclopedia of Genes and Genomes (KEGG) pathway analyses was performed using the ShinyGO version 0.77 tool (South Dakota State University, United States of America)[47].

Statistics

All statistical analyses and visualization of data was performed using Prism 9 (GraphPad, San Diego, CA) software. Viral titer and relative mRNA expression data values were log-transformed prior to statistical analysis. Statistical tests were performed as indicated by figure legends including Student's t-test, one-way analysis of variance (ANOVA) with Tukey's multiple comparisons test, and two-way ANOVA with Sidak's or Dunnett's multiple correction test as appropriate. The Shapiro-Wilk test was applied to each dataset to test for normality determination to confirm appropriateness of parametric tests. One-tailed testing was used unless otherwise specified, and error bars represent the standard deviation (SD). A P-value less than 0.05 was considered statistically significant throughout this study.

Data availability

All raw data have been deposited at Mendeley Data and are publicly available as of the date of publication (https://doi.org/10.17632/75fb98r6xh.1). This paper does not report original code. Generated RNA-sequencing data has been deposited in NCBI-Gene Expression Omnibus database and will be available as of the date of publication. Any additional information required to reanalyze the data reported in this paper can be requested from the primary author (Boaz Wong, email: boaz.wong@uottawa.ca).

Received: 16 January 2024; Accepted: 17 October 2024
Published online: 16 November 2024

References

1. Kelly, E. & Russell, S. J. History of oncolytic viruses: Genesis to genetic engineering. *Mol. Ther.* **15**, 651–659 (2007).
2. Rehman, H., Silk, A. W., Kane, M. P. & Kaufman, H. L. Into the clinic: Talimogene laherparepvec (T-VEC), a first-in-class intratumoral oncolytic viral therapy. *J. Immunother Cancer*. **4**, 53 (2016).
3. Russell, S. J., Peng, K. W. & Bell, J. C. Oncolytic virotherapy. *Nat. Biotechnol.* **30**, 658–670 (2012).
4. Katze, M. G., He, Y. & Gale, M. Viruses and interferon: A fight for supremacy. *Nat. Rev. Immunol.* **2**, 675–687 (2002).
5. Matveeva, O. V. & Chumakov, P. M. Defects in interferon pathways as potential biomarkers of sensitivity to oncolytic viruses. *Rev. Med. Virol.* **28**, 6 (2018).
6. Forbes, N. E., Abdelbary, H., Lupien, M., Bell, J. C. & Diallo, J. S. Exploiting tumor epigenetics to improve oncolytic virotherapy. *Front. Genet.* **4**, (2013).
7. Forbes, N. E., Krishnan, R. & Diallo, J. S. Pharmacological modulation of Anti-tumor Immunity Induced by Oncolytic Viruses. *Front. Oncol.* **4**, 191 (2014).
8. Selman, M. et al. Multi-modal potentiation of Oncolytic Virotherapy by Vanadium compounds. *Mol. Ther.* **26**, 56–69 (2018).
9. Wong, B. et al. Dependency of EGFR activation in vanadium-based sensitization to oncolytic virotherapy. *Mol. Ther. - Oncolytics*. **25**, 146–159 (2022).
10. Vlastaridis, P. et al. Estimating the total number of phosphoproteins and phosphorylation sites in eukaryotic proteomes. *GigaScience* 6, (2017).
11. Carbone, C. J. et al. Protein tyrosine phosphatase 1B is a key regulator of IFNAR1 endocytosis and a target for antiviral therapies. *Proc. Natl. Acad. Sci.* 109, 19226–19231 (2012).
12. An, H. et al. Phosphatase SHP-1 promotes TLR- and RIG-I-activated production of type I interferon by inhibiting the kinase IRAK1. *Nat. Immunol.* **9**, 542–550 (2008).
13. Martin, N. T. & Bell, J. C. Oncolytic virus combination therapy: killing one bird with two stones. *Mol. Ther.* **26**, 1414–1422 (2018).
14. Bourgeois-Daigneault, M. C. et al. Oncolytic vesicular stomatitis virus expressing interferon-σ has enhanced therapeutic activity. *Mol. Ther. - Oncolytics*. **3**, 16001 (2016).
15. Veinalde, R. et al. Oncolytic measles virus encoding interleukin-12 mediates potent antitumor effects through T cell activation. *OncoImmunology*. **6**, e1285992 (2017).
16. Wong, B. et al. Optimal delivery of RNA interference by viral vectors for cancer therapy. *Mol. Ther.***S1525001623004999**. https://doi.org/10.1016/j.ymthe.2023.09.012 (2023).
17. Garcia, V. et al. High-throughput titration of luciferase-expressing recombinant viruses. *J. Vis. Exp.* **51890**. https://doi.org/10.3791/51890 (2014).
18. Rehwinkel, J. & Gack, M. U. RIG-I-like receptors: their regulation and roles in RNA sensing. *Nat. Rev. Immunol.* **20**, 537–551 (2020).

19. Mannan, A. U. et al. Mutation in the gene encoding lysosomal acid phosphatase (Acp2) causes cerebellum and skin malformation in mouse. *Neurogenetics*. **5**, 229–238 (2004).
20. Bailey, K., Rahimi Balaei, M., Mehdizadeh, M. & Marzban, H. Spatial and temporal expression of lysosomal acid phosphatase 2 (ACP2) reveals dynamic patterning of the mouse cerebellar cortex. *Cerebellum*. **12**, 870–881 (2013).
21. Waheed, A., Van Etten, R. L., Gieselmann, V. & Von Figura, K. Immunological characterization of human acid phosphatase gene products. *Biochem. Genet.* **23**, 309–319 (1985).
22. Makrypidi, G. et al. Mannose 6 dephosphorylation of Lysosomal Proteins Mediated by Acid Phosphatases Acp2 and Acp5. *Mol. Cell. Biol.* **32**, 774–782 (2012).
23. Lee, J., Kim, J., Son, K. & Min, J. Y. d'Alexandry d'Orengiani, A.-L. P. H. Acid phosphatase 2 (ACP2) is required for membrane fusion during influenza virus entry. *Sci. Rep.* 7, 43893 (2017).
24. Eden, E., Navon, R., Steinfeld, I., Lipson, D. & Yakhini, Z. GOrilla: a tool for discovery and visualization of enriched GO terms in ranked gene lists. *BMC Bioinform.* **10**, 48 (2009).
25. Eden, E., Lipson, D., Yogev, S. & Yakhini, Z. Discovering motifs in ranked lists of DNA sequences. *PLoS Comput. Biol.* **3**, e39 (2007).
26. Naik, R. R., Shakya, A. K., Aladwan, S. M. & El-Tanani, M. Kinase inhibitors as potential therapeutic agents in the treatment of COVID-19. *Front. Pharmacol.* **13**, 806568 (2022).
27. Zhang, Z. Y. Drugging the Undruggable: therapeutic potential of targeting protein tyrosine phosphatases. *Acc. Chem. Res.* **50**, 122–129 (2017).
28. Mullard, A. Phosphatases start shedding their stigma of undruggability. *Nat. Rev. Drug Discov.* **17**, 847–849 (2018).
29. Okabe, Y., Sano, T. & Nagata, S. Regulation of the innate immune response by threonine-phosphatase of eyes absent. *Nature*. **460**, 520–524 (2009).
30. Gu, M. et al. Protein phosphatase PP1 negatively regulates the toll-like receptor- and RIG-I-like receptor-triggered production of type I interferon by inhibiting IRF3 phosphorylation at serines 396 and 385 in macrophage. *Cell. Signal.* **26**, 2930–2939 (2014).
31. Wang, L. et al. Protein phosphatase 1 abrogates IRF7-mediated type I IFN response in antiviral immunity. *Eur. J. Immunol.* **46**, 2409–2419 (2016).
32. Shanker, V., Trincucci, G., Heim, H. M. & Duong, H. T. F. Protein phosphatase 2A impairs IFNα-induced antiviral activity against the hepatitis C virus through the inhibition of STAT1 tyrosine phosphorylation. *J. Viral Hepat.* **20**, 612–621 (2013).
33. Koyama, M. et al. Phosphorylation of CPI-17, an inhibitory phosphoprotein of smooth muscle myosin phosphatase, by rho-kinase. *FEBS Lett.* **475**, 197–200 (2000).
34. Zhan, Z. et al. Phosphatase PP4 negatively regulates type I IFN production and antiviral innate immunity by Dephosphorylating and deactivating TBK1. *J. Immunol.* **195**, 3849–3857 (2015).
35. Sun, X., Roth, S. L., Bialecki, M. A. & Whittaker, G. R. Internalization and fusion mechanism of vesicular stomatitis virus and related rhabdoviruses. *Future Virol.* **5**, 85–96 (2010).
36. Katze, M. G., Fornek, J. L., Palermo, R. E., Walters, K. A. & Korth, M. J. Innate immune modulation by RNA viruses: emerging insights from functional genomics. *Nat. Rev. Immunol.* **8**, 644–654 (2008).
37. Chang, K., Marran, K., Valentine, A. & Hannon, G. J. Creating an miR30-Based shRNA Vector. *Cold Spring Harb. Protoc.* pdb. prot075853 (2013). (2013).
38. Gordon, J. A. [41] Use of vanadate as protein-phosphotyrosine phosphatase inhibitor. in Methods in Enzymology vol. 201 477–482 (Elsevier, (1991).
39. Stojdl, D. F. et al. VSV strains with defects in their ability to shutdown innate immunity are potent systemic anti-cancer agents. *Cancer Cell.* **4**, 263–275 (2003).
40. Diallo, J. S., Vähä-Koskela, M., Le Boeuf, F. & Bell, J. Propagation, purification, and in vivo testing of oncolytic vesicular stomatitis virus strains. **797**, 127–140 (2012).
41. Diallo, J. S. et al. A high-throughput Pharmacoviral Approach identifies Novel Oncolytic Virus Sensitizers. *Mol. Ther.* **18**, 1123–1129 (2010).
42. Pfaffl, M. W. A new mathematical model for relative quantification in real-time RT-PCR. *Nucleic Acids Res.* **29**, 45e–445 (2001).
43. Bray, N. L., Pimentel, H., Melsted, P. & Pachter, L. Near-optimal probabilistic RNA-seq quantification. *Nat. Biotechnol.* **34**, 525–527 (2016).
44. Pimentel, H., Bray, N. L., Puente, S., Melsted, P. & Pachter, L. Differential analysis of RNA-seq incorporating quantification uncertainty. *Nat. Methods*. **14**, 687–690 (2017).
45. Sales, G., Calura, E., Cavalieri, D. & Romualdi, C. Graphite - a Bioconductor package to convert pathway topology to gene network. *BMC Bioinform.* **13**, 20 (2012).
46. Martini, P., Sales, G., Massa, M. S., Chiogna, M. & Romualdi, C. Along signal paths: an empirical gene set approach exploiting pathway topology. *Nucleic Acids Res.* **41**, e19–e19 (2013).
47. Ge, S. X., Jung, D. & Yao, R. ShinyGO: a graphical gene-set enrichment tool for animals and plants. *Bioinformatics*. **36**, 2628–2629 (2020).

Acknowledgements

The authors would like to thank Dr. David Cook (University of Ottawa) for his guidance throughout the RNA sequencing analysis. The authors would also like to acknowledge Donnelly Sequencing Centre (http://ccbr.utoronto.ca/donnelly-sequencing-centre) for their efficiency and professionalism in providing their RNA-sequencing service.

Author contributions

Conceptualization: BW, AB, RA, JSDMethodology: BW, RB, AB, RA, CI, JSDInvestigation: BW, RB, AB, KN, GM, AC, AL, MC, RAVisualization: BW, KNFunding acquisition: CI, JSDProject administration: BW, RA, JSD-Supervision: RA, CI, JSDWriting – original draft: BW, RB, RAWriting – review & editing: BW, RB, RA, CI, JSDAll authors reviewed the manuscript.

Funding

Terry Fox Research Institute, TFF-122868 (JSD). Canadian Institutes of Health Research, grant INI-147824 (JSD). Canadian Institutes of Health Research, grant #705952 (JSD). Canadian Cancer Society supported by the Lotte & John Hecht Memorial Foundation, grant #703014 (JSD). Canadian Institutes of Health Research, Canada Graduate Scholarship Doctoral (CGS-D) Award (BW).

Declarations

Competing interests
The authors declare no competing interests.

Additional information
Supplementary Information The online version contains supplementary material available at https://doi.org/10.1038/s41598-024-76855-3.

Correspondence and requests for materials should be addressed to J.-S.D.

Reprints and permissions information is available at www.nature.com/reprints.

Publisher's note Springer Nature remains neutral with regard to jurisdictional claims in published maps and institutional affiliations.